Proceedings of ASME Turbo Expo 2011
GT2011
June 6-10, 2011, Vancouver, British Columbia, Canada

GT2011-45146

TURBULENT CONVECTION FROM DETERMINISTIC ROUGHNESS DISTRIBUTIONS WITH VARYING THERMAL CONDUCTIVITIES

Steven R. Mart
Graduate Student
Mechanical Engineering Department
Baylor University
Waco, TX 76798-7356

Stephen T. McClain
Assistant Professor
Mechanical Engineering Department
Baylor University
Waco, TX 76798-7356

Lesley M. Wright
Assistant Professor
Mechanical Engineering Department
Baylor University
Waco, TX 76798-7356

ABSTRACT

Many flows of engineering interest are bounded by surfaces that exhibit roughness with thermal conductivities much lower than common metals and alloys. Depending on the local roughness element convection coefficients, the low thermal conductivities of the roughness elements may create situations where temperature changes along the heights of the elements are important and must be considered in predicting the overall surface convection coefficient. The discrete-element model (DEM) for flows over rough surfaces was recently adapted to include the effects of internal conduction along the heights of ordered roughness elements. While the adapted DEM provided encouraging agreement with the available data, more data are required to validate the model. To further investigate the effects of roughness element thermal conductivity on convective heat transfer and to acquire more experimental data for DEM validation, four wind tunnel test plates were made. The test plates were constructed using Plexiglas and Mylar film with a gold deposition layer creating a constant flux boundary condition with steady state wind tunnel measurements. The four test plates were constructed with hexagonal distributions of hemispheres or cones made of either aluminum or ABS plastic. The plates with hemispherical elements had element diameters of 9.53 mm and a spacing-to-diameter ratio of 2.099. The plates with conical elements had base element diameters of 9.53 mm and a spacing-to-base-diameter ratio of 1.574. An infrared camera was used to measure the temperature of the heated plates in the Baylor Subsonic Wind Tunnel for free stream velocities ranging from 2.5 m/s to 35 m/s (resulting in Reynolds number values ranging from 90,000 to 1,400,000 based on the distance from the knife-edge to the center of the infrared camera image) in turbulent flow. At lower Reynolds numbers, the thermal conductivity of the roughness elements is a primary factor in determining the heat transfer enhancement of roughness distributions. At the higher Reynolds numbers investigated, the hemispherical distribution, which contained more sparsely spaced elements, did not exhibit a statistically significant difference in enhancement for the different thermal conductivity elements used. The results of the study indicate that the packing density of the elements and the enhancement on the floor of the roughness distribution compete with the roughness element thermal conductivity in determining the overall convection enhancement of rough surfaces.

INTRODUCTION

While most turbine blades are highly polished when they enter service, the in-service development of roughness for land-based, aviation, and marine turbine blades and engine surfaces has been demonstrated by several studies. References [1-3] are three examples that demonstrate the multiple order of magnitude increase in roughness statistics for aviation and land-based turbine surfaces after normal operational lives. The increase in surface roughness increases flow resistance and increases heat transfer from the combustion products to the engine surfaces. The increased friction and heat transfer combine to lower performance and reduce the operational life of the components.

Bons et al. [1] showed that roughness on gas turbine blades is caused by, among other things, spallation of thermal barrier coatings or by fuel deposits that solidify after impinging the turbine blades. Modern thermal barrier coatings have thermal conductivities on the order of 1.5 W/m·K at temperatures around 1200 K [4-6], which is much less than the thermal conductivity of the turbine blade material [7]. Fuel deposits which may be composed of ceramic oxides or inter-metallics are also expected to exhibit thermal conductivities much less than their superalloy substrates. Because of the lower thermal conductivities of different roughness exhibited in gas turbines, temperature change along the heights of the roughness elements is expected to occur as the roughness elements protrude into the velocity and thermal boundary layers.

The discrete-element model (DEM) for flows over rough surfaces presents a spatially averaged option for evaluating convective heat transfer from rough surfaces that includes the effects of roughness element thermal conductivity. The basis for the discrete-element model (DEM) for flows over rough surfaces was first described by Schlichting in his classic 1937 paper [8]. In attempting to explain the effect of roughness element packing density on the effective sand-grain height, Schlichting suggested that the total drag on a rough surface is the sum of skin friction on the flat part of the surface and the form drag on the individual roughness elements. Regarding heat transfer, Schlichting's concept can be extended as the total flux from a rough surface is the sum of heat transfer from the flat part of the surface and the heat transfer from the individual roughness elements.

The form of the discrete-element roughness model most commonly used originated in the work of Finson [9] and was rigorously derived by Taylor [10]. In the discrete-element model, the effects of the roughness elements: decreased flow area, the drag on the roughness elements, and the heat transferred from the roughness elements to the flow stream, are evaluated by solving equations of fluid motion specifically derived to include the effects [10]. The DEM is a spatially averaged model, so while the information about the roughness elements must be resolved in the direction normal to the solid wall, the roughness element shape information is not resolved in the two directions parallel to the solid wall.

By incorporating the effect of the roughness elements into the equations of fluid mechanics, the DEM captures important physics of flow over rough surfaces based on integral quantities of the boundary layer while requiring much less computational storage and time than direct numerical simulations that fully resolve the roughness elements and the flow field [11]. However, the DEM is semi-empirical in that correlations, based on experimental data for flows over banks of cylinders, are used to describe the drag and heat transfer interactions of the roughness elements protruding into the fluid. While correlations are used for the local element drag and local element heat transfer to the fluid, the DEM has a significant advantage over methods such as the equivalent-sand grain approach in that realistic temperature changes along the height of the elements can be considered in evaluating the heat transfer.

McClain et al. [12] recently adapted the discrete-element model to include the effect of temperature changes along the heights of ordered roughness elements with finite thermal conductivities. Two methods for capturing the effects of temperature changes along the heights of the roughness elements were presented by McClain et al. [12]. The first method involved using a fin efficiency. While the fin-efficiency approach was computationally inexpensive when implemented in a boundary layer code, the approach requires knowing the fin efficiency *a priori*. The second approach was a conjugate scheme where a fin-equation integrator was incorporated into a boundary layer code and the fin equation and the boundary layer equations were solved simultaneously. While both methods were found to be successful in different aspects, only three experimental measurements of convection from rough surfaces with low thermal conductivity were available for validation. To advance either approach, more experimental measurements of convection from rough surfaces with high and low thermal conductivity elements are required.

The objectives of this study were to investigate the effects of element thermal conductivity on turbulent convection from rough surfaces using ordered, deterministic roughness elements on a flat plate. These distributions characteristics were chosen to represent the types of features expected for turbine blade roughness caused by foreign contaminant deposition. The first set of plates involved hemispheres in a closely packed hexagonal arrangement with a spacing to diameter ratio of 2.099. The second set of plates involved cones in a more closely packed hexagonal arrangement with a spacing to diameter ratio of 1.574. The ratio of the roughness height to the location of the thermal measurements from the leading edge was 0.0073. This ratio is an order of magnitude larger than the roughness to axial chord ratios expected for erosion or corrosion blade roughness [13], but is representative of the relative roughness heights measured for deposition roughness on land-based high-pressure turbine blades for power generation [1]. Further, the geometries were chosen to provide very similar Sigal-Danberg parameters [14] as evaluated using the modifications of McClain et al. [15] which consider the features of the roughness elements above the distribution mean elevation.

For each roughness distribution geometry, two test plates were constructed: one plate with aluminum elements (k_R = 180 W/m·K) and another plate with ABS plastic elements (k_R = 0.18 W/m·K). This range of thermal conductivities was chosen to bound the expected ranges of thermal conductivities for deposition roughness whether the source of the deposition elements is sand, inter-metallic particles, or ceramic oxides.

METHODOLOGY

To investigate the importance of the element thermal conductivity in determining roughness distribution convection heat transfer enhancement, a series of experiments were performed in the Baylor University Subsonic Wind Tunnel

(Model 406) which was manufactured by Engineering Laboratory Design, Inc. The wind tunnel test section has a cross-section of 60.96 cm x 60.96 cm (24 in. by 24 in.) and uses a 40 HP electric motor that drives a constant pitch fan. The variable speed motor can produce a flow ranging from a low velocity of 0.1 m/s to an upper tunnel velocity greater than 50 m/s and the velocity variation over the test section is less than ±1 %. An inlet contraction ratio of 6.25:1, a precision honeycomb inlet, and three graduated, high-porosity screens provide a clean inlet turbulence intensity of approximately 0.2%.

The four test plates used in this study measured 1.91 cm by 60.96 cm by 91.44 cm (0.75 in. by 24 in. by 36 in.) and were constructed out of Plexiglas. A constant heat flux was applied to each of the plates using a sheet of gold deposited Mylar film oriented "gold side" down. This orientation allowed for the attachment of roughness elements to the insulated side of the Mylar sheet without disrupting the constant flux heating condition it provides. Each test plate was constructed with a hexagonal distribution of either hemispherical or conical roughness elements constructed from 6061 aluminum alloy (k_R = 180 W/m·K) or ABS plastic (k_R = 0.18 W/m·K). The two plates with hemispherical distributions had element diameters of 9.53 mm and a spacing-to-diameter ratio of 2.099. The two plates with conical distributions had base element diameters of 9.53 mm and a spacing-to-base-diameter ratio of 1.574. The first row of the every distribution was placed 0.471 meters from the knife edge of the plate. **Table 1** summarizes the roughness descriptions for the four distributions investigated. Following construction of each plate, the plate was painted with a flat-black paint with a manufacturer reported emissivity of 0.95.

Table 1. Summary of Roughness Parameters for Distributions Investigated

Parameter	Plastic Hemispheres	Aluminum Hemispheres	Plastic Cones	Aluminum Cones
D (mm)	9.530	9.530	9.530	9.530
k (mm)	4.765	4.765	4.765	4.765
S (mm)	20	20	15	15
Δy_m (mm)	0.654	0.654	0.581	0.581
k_{eff} (mm)	4.111	4.111	4.183	4.183
Λ_{eff}	38.0	38.0	39.9	39.9
k_R (W/m·K)	0.18	180	0.18	180

Each test plate was mounted in the Baylor University Subsonic Wind Tunnel and a series of two tests were performed. The first set of measurements used a FLIR ThermaCam SC4000 infrared camera to generate highly resolved thermal mappings of the test surface. The SC4000 used in this study has a 320 by 256 pixel resolution indium antimonide (InSb) detector. The accuracy of any surface temperature measurement is reported by FLIR as 0.09 K for temperatures near standard atmospheric conditions [16]. Using a 25-mm lens at a distance of approximately 36 cm from the heated surface, the width of each pixel represented a width of 0.467-mm on the heated surfaces. This pixel width enabled twenty temperature measurements to be taken across the diameter of each roughness element. The total viewing area of the infrared plate image spanned 14.9 cm in the flow direction and 12.0 cm in the spanwise direction.

The second set of measurements used a hot wire anemometry system to obtain the unheated velocity boundary layer thickness between two rows of the roughness distribution. These two investigations were performed for nominal velocities of 2.5 to 35 meters per second. After this test cycle was completed, a new plate was mounted in the wind tunnel and the measurements were repeated for the three remaining test plates.

For each of these experiments, a Type T thermocouple with an Omega Cold Junction Compensator was used to measure the freestream temperature, a Siemens QFM3101 Relative Humidity Sensor measured the relative humidity in the laboratory, and an Oakton barometer was used to measure the laboratory atmospheric pressure. The freestream velocity was measured using a 15.24 cm Pitot-static probe. Because of the large range of velocities tested, a large range of dynamic pressures were measured. Therefore, two different transducers were used to measure the dynamic pressure difference experienced by the Pitot probe. For the low velocity tests, an Omega PCL-2A pressure transducer with a range of 0-2 in. of H_2O and an absolute accuracy of .0012 in. of H_2O was used. For tests over 20 m/s, a Mamac Systems PR-274-R3-VDC pressure transducer was used to measure the dynamic pressure.

For the infrared measurements, an Omega Cold Junction Compensator with a Type K thermocouple was used to measure the temperature of the base of the Plexiglas plate directly below the roughness elements. A Newport HHM290 TrueRMS Supermeter measured the voltage supplied to the test plate, and a Fluke Y8100 DC/AC Current Probe (2% absolute accuracy) measured the current supplied to the test plate. With the exception of the Oakton Barometer, Newport HHM290 TrueRMS Supermeter, and Fluke Y8100 DC/AC Current Probe, all of the measurements were acquired using a Dell Optiplex GX260 computer with National Instruments (NI) LabVIEW 7.1 software and a PCI-6052 E Multifunction DAQ card.

Figure 1 presents a side view of the wind tunnel test section and indicates the locations of the roughness distribution, the infrared camera, and the hot-wire probe relative to the knife-edge of the test plate. The following sections discuss the experimental methods and procedures of each test.

Surface Temperature Maps

For this test, the FLIR SC4000 Infrared Camera was used to monitor the surface temperature of the test plate. To minimize any radiative effects from the lights within the room, the test section was covered with black felt. As mentioned previously, the dynamic pressure, relative humidity, freestream temperature, and Plexiglas temperature were acquired continuously using a LabVIEW driven data acquisition system measuring 10,000 samples at a rate of 200,000 samples per second. The average value and random uncertainty for each of these measurements were written to a summary file.

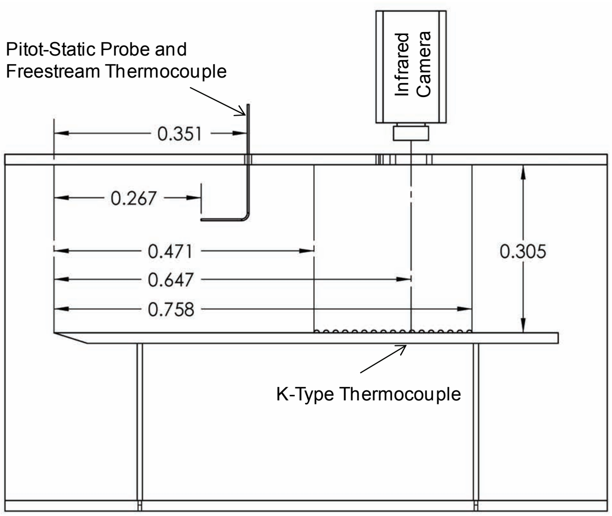

Figure 1. Side View of Wind Tunnel Test Section (all dimensions in meters)

An *in-situ* calibration was used to reference the freestream thermocouple and the Plexiglas thermocouple to the infrared camera measurement of the unheated plate temperature in ambient laboratory conditions. To begin the process, a 100-frame, one-point correction was performed using the infrared camera software. Then, a two second infrared video at 30 frames per second was acquired while simultaneously sampling from the freestream thermocouple and the thermocouple attached to the bottom of the Plexiglas plate. The difference between each of the thermocouple measurements and the mean infrared temperature measurement during the calibration period was subtracted from each respective thermocouple measurement during the tests. This procedure was performed prior to each day of testing.

Following the *in-situ* calibration, the plate was heated using three BK Precision 1761 power supplies wired in parallel. Starting with a wind tunnel velocity of 2.5 m/s, the plate's temperature was continuously monitored. The settings on the power supplies were set to provide a temperature difference between the plate and the freestream of approximately 15 K. Then, every 10 minutes, an infrared video of the roughness elements was taken for two seconds at a rate of 30 frames per second and the power settings and atmospheric pressure were recorded manually. Once steady state conditions were confirmed by comparing the change in the measured mean surface temperature to the uncertainty in the temperature measurement, a final infrared video was taken. After the final infrared temperature measurement, the wind tunnel velocity was set to the next speed, the settings on the power supplies were adjusted, and the temperature measurement process was repeated.

Velocity Boundary Layer Profiles

To acquire velocity boundary layer profiles, a Model 1201 hot film probe was powered by a TSI Inc. IFA 300 Constant Temperature Anemometry system. A Dell Optiplex GX1 computer using ThermalPro software was used to initialize the IFA300 and to assign a channel to the probe.

The hot-wire probe was mounted to a Velmex Inc. BiSlide/Unislide assembly used for two-dimensional traversing. Using a Velmex Inc. Stepping Controller, the hot-wire probe was positioned at the center of the infrared image between two roughness rows and below the apex of a roughness element. The initial placement of the hotwire probe was within 2 mm from the surface floor.

Starting with a velocity of 2.5 m/s, the traversing system was used to move the probe through a geometrically expanding grid to construct the boundary layer profiles. Once at steady state conditions, the LabVIEW driven stepper motors moved the hot-wire probe through a 6-inch, 101-station, geometrically expanding measurement grid with a geometric expansion factor of 1.07.

For the hemispherical elements, five traces were acquired for each freestream velocity. The five traces were taken at one x-location from the leading edge located between roughness element rows near the center of the infrared camera imaging region. The five traces spanned one full element spacing. That is, the first trace was directly between two roughness elements. Following each trace, the probe was moved ¼ of the element spacing in the spanwise direction.

For the plates with conical roughness elements, which were spaced more closely than the hemispherical elements, a spanwise scan of five traces could not be made at higher velocities. For freestream velocities over 15 m/s, deflection of the hot-wire probe and support was significant enough that interference or contact with the elements in the downstream row was possible. Consequently, only on trace centered between elements and rows was taken at each freestream velocity.

At each measurement station, a United Electronic Industries (UEI) PD2-MFS-4-300/16 PowerDAQ installed on the GX260 was used to acquire 200,000 raw voltages across the probe acquired at a rate of 200,000 samples per second. Additionally, 10,000 samples of the dynamic pressure, relative humidity, and freestream temperature were also taken at 200,000 samples per second. Again, the average value and random uncertainty for each of these measurements were written to a summary file. The raw hot-wire voltage measurements at each station were also recorded for post processing.

Atmospheric pressure within the room was recorded at the start and the completion of each trace. Once the full scan was completed, the wind tunnel velocity was increased and the process was repeated.

DATA REDUCTION AND PROCESSING

Both of the measurement sets required unique methods for data reduction. In the following sections, the data reduction methods are described. When available, validations of the measurement methods are also provided.

Infrared Measurement Processing

The steady state infrared videos and the calibration videos, each of approximately 60 frames, were averaged at each pixel to begin the analysis. While the manufacturer reported uncertainty of any temperature measurement using the camera is 0.09 K, evaluating the mean temperature at each pixel location over the 60-frame steady state video allowed the random uncertainty of each infrared temperature measurement to be reduced to below 0.01 K.

At each freestream velocity, the average convection coefficient was determined using Eq. (1).

$$\bar{h} = \left(\frac{\frac{E \cdot I}{A_p}\frac{t_P}{k_P} - \left(\bar{T} - T_P\right)}{\left(\bar{T} - T_\infty\right)} \right)\left(\frac{t_M}{k_M} + \frac{\Delta y_m}{k_R} + \frac{t_P}{k_P} \right)^{-1} - \frac{\varepsilon\sigma\left(\bar{T}^4 - T_w^4\right)}{\left(\bar{T} - T_\infty\right)} \quad (1)$$

Eq. (1) corrects for the conduction through the Plexiglas plate, the conduction through the Mylar sheet with roughness, and the radiation from the heated surface to the ambient surroundings. For the experiments, the conduction through the Plexiglas and the radiation to the surroundings are important. At the high freestream velocities studied, approximately 10% of the energy dissipated by the gold foil exits through the Plexiglas, while 4% of the energy dissipated by the gold foil leaves as radiation from the plate. For the low freestream velocities, these effects become increasingly important because of the lowered convection coefficients. For the lowest freestream velocity studied (2.5 m/s), approximately 20% of the energy dissipated by the gold foil exits through the Plexiglas, while 19% of the energy leaves as radiation.

The uncertainties of the measured convection coefficients and resulting Frossling numbers or Stanton numbers were determined using the large sample size approach of Coleman and Steele [17] which has its origin in the method of Kline and McClintock [18]. **Table 2** presents the uncertainties in the measured quantities used to determine the average convection coefficients determined using Eq. (1).

In Eq. (1), the conductance of the roughness elements is evaluated as the "melt-down height" divided by the thermal conductivity of the roughness elements. In considering the roughness elements as a bank of fins, one might also employ a finned surface conductance similar to $\left(1/\eta_0 h\right)$, where η_0 is the overall surface efficiency and h is the average convection coefficient [19]. Issues with the overall surface efficiency approach are 1) the efficiency of an individual roughenss element must be known *a priori*, 2) the convection coefficient must be constant along the entire surface and must be known *a priori*, and most importantly, 3) surface temperature must be constant and unaffected by the presence of the fins. None of these requirements is met for roughness elements immersed in a turbulent boundary layer.

To validate the temperature measurement systems, the average convection coefficient on a flat plate with unperturbed (smooth) regions were also determined for freestream velocities of 0.7 m/s to 35 m/s (see Ref. [20] for details of the unperturbed plate validation). **Figure 2** presents the measured heat transfer coefficients on the unperturbed regions of the plate in the form of Frossling numbers where,

$$Fr_x = \frac{Nu_x}{\sqrt{\mathrm{Re}_x}} \quad (2)$$

Table 2. Measurement Uncertainties Employed in the Evaluation of Heat Transfer Coefficient Uncertainties

Var.	Instrument	Uncertainty
T_∞	T-type thermocouple	$\left(\left(\frac{tS_{T_\infty}}{\sqrt{N}}\right)_{meas}^2 + \left(\frac{tS_{T_\infty}}{\sqrt{N}}\right)_{cal}^2 + \left(\frac{tS_{\bar{T}}}{\sqrt{N}}\right)_{cal}^2 + (0.09K)^2\right)^{0.5}$
$\bar{T}$	FLIR SC4000	$\left(\left(\frac{tS_{\bar{T}}}{\sqrt{N}}\right)_{meas}^2 + \left(\frac{tS_{\bar{T}}}{\sqrt{N}}\right)_{cal}^2 + (0.09K)^2\right)^{0.5}$
T_P	K-type thermocouple	$\left(\left(\frac{tS_{T_P}}{\sqrt{N}}\right)_{meas}^2 + \left(\frac{tS_{T_P}}{\sqrt{N}}\right)_{cal}^2 + \left(\frac{tS_{\bar{T}}}{\sqrt{N}}\right)_{cal}^2 + (0.09K)^2\right)^{0.5}$
E	Newport HHM290	1% of reading
I	Fluke Y8100	2% of FS = 0.4 A
A_p	Meter stick	2 mm for each dimension
t_P	Manuf. Spec.	0.05 mm
t_M	Manuf. Spec.	0.003 mm

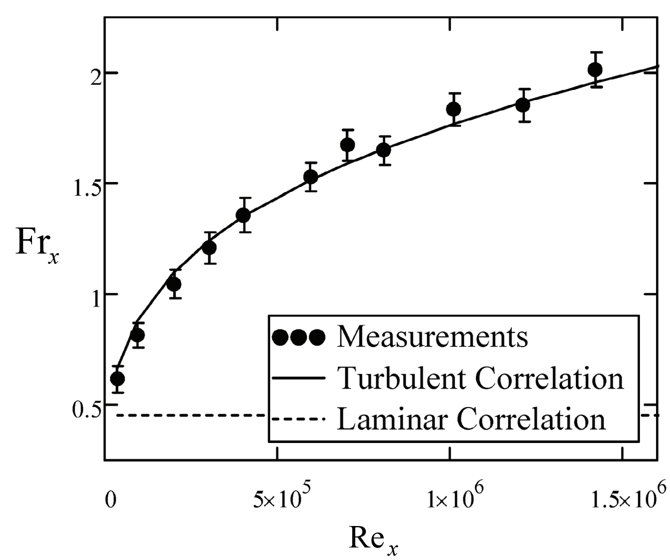

Figure 2. Frossling Number Comparison of the Unperturbed Sections of a Smooth Test Plate

Figure 2 further presents a comparison of the measured Frossling numbers to the values predicted by traditional constant-wall flux Nusselt number correlations for turbulent flow (Eq. 3) and for laminar flow (Eq. 4) neglecting the unheated starting length [21].

$$\mathrm{Nu}_x = 0.0308\,\mathrm{Re}_x^{4/5}\,\mathrm{Pr}^{1/3} \tag{3}$$

$$\mathrm{Nu}_x = 0.453\,\mathrm{Re}_x^{1/2}\,\mathrm{Pr}^{1/3} \tag{4}$$

Figure 2 demonstrates that with the exception of two flow conditions, the measured Frossling numbers agree with the values predicted by the turbulent correlation. That is, the uncertainty bars of the measured Frossling numbers includes the values predicted by the correlation. When the uncertainties of the measured Frossling numbers do not include the correlation predictions, the maximum percentage difference between the two is 6% of the correlation value.

Velocity Boundary Layer Analyses

For flow over smooth surfaces, the Clauser approach [22] may be used to simultaneously evaluate the initial elevation of the probe from the wall. For rough surfaces, Coleman et al. [23] suggested that the logarithmic region of a fully-rough flow is described by

$$\frac{u}{u^*} = \frac{1}{\kappa}\ln\left(\frac{y'-\xi}{k}\right) + A \tag{5}$$

where y' is the height above the mean elevation, ξ is the frictional offset height, and

$$u^* = U_\infty\sqrt{\frac{C_f}{2}} \tag{6}$$

Eqns. (5) and (6) indicate that when only one (u) mean velocity profile from a single-wire probe is employed, there are in essence four unknowns 1) the initial height of the probe from the wall, 2) the frictional offset height, 3) the log region intercept, and 4) the skin friction coefficient. Since the logarithmic region is described by at most two constants (for example, 1/κ and the intercept), the system is under-constrained and the important frictional properties of the flow cannot be directly determined.

While the Clauser approach cannot identify the initial hot-wire probe height, the integral boundary layer quantities may be evaluated if an alternative method is used to register the initial height of the hot wire probe. Because the hotwire probe was started well below the peaks of the roughness elements, either the mean velocity or the local turbulence intensity profiles may be inspected to determine the initial probe offset height. More specifically, based on changes in the velocity profile or the turbulence intensity profile, the elevation of the roughness element apices in the hot-wire traces could be identified and used to determine the initial probe position.

Figures 3 and 4 demonstrate the changes in velocity and turbulence intensity profiles for 15 m/s flow over the hemispherical elements. These figures show that as the hot-wire probe rose above the apices of the roughness elements, a change in slope of the profiles is observed. Figure 4 demonstrates that below the apices of elements, the turbulence intensity either rapidly increases (if in the separation-and-reattachment region behind a roughness element) or remains essentially constant as the probe is moved nearer to the wall. In Figures 3 and 4 all of these effects are observable. For some of the velocity profile traces, only one of the effects was readily apparent. For the cone distribution traces, which did not involve multiple traces in the spanwise direction, the turbulence intensity profile was the predominant method used to register the initial height of the hot-wire probe.

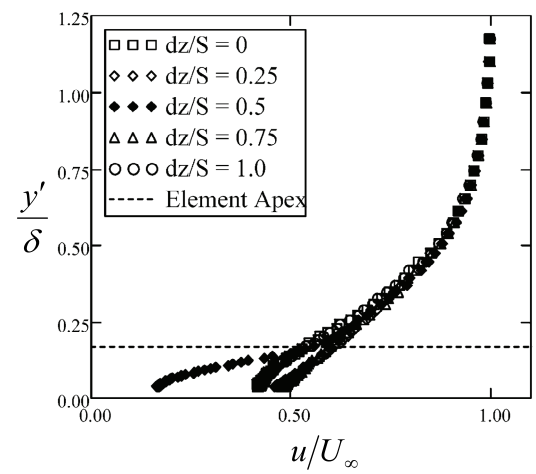

Figure 3: Comparison of Viscous Boundary Layer Traces on the Plastic Hemispherical Plate at 15 m/s

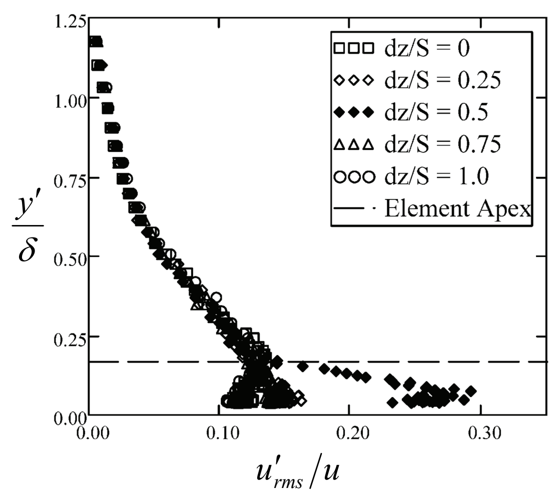

Figure 4: Comparison of Boundary Layer Turbulence Intensities on the Plastic Hemispherical Plate at 15 m/s

Once the initial profile offset heights were determined, the 99% boundary layer thickness (δ) was determined for each velocity profile. The integral boundary layer parameters (δ^*, θ_M) were determined using Eqns. (7) and (8).

$$\delta^* = \int_{y=0}^{y=\delta} \left(1 - \frac{u}{U_\infty}\right) dy \tag{7}$$

$$\theta_M = \int_{y=0}^{y=\delta} \frac{u}{U_\infty}\left(1 - \frac{u}{U_\infty}\right) dy \tag{8}$$

For each of the roughness geometries, only the velocity profiles measured for the plastic elements are presented. Velocity boundary layer measurements were made for both the plastic and aluminum cones for velocities less than 17.5 m/s. The differences between the velocity boundary layer measurements for the cone surfaces were well within the experimental uncertainties of the measurements used.

RESULTS AND DISCUSSION

Table 3 presents the heat transfer parameters measured during the infrared tests for the plates with hemispherical elements, while **Table 4** presents the same information for the plates with conical elements. The measured convection coefficients and their uncertainties are presented in **Table 5**. **Table 6** presents a summary of the velocity and heat transfer measurements for the hemispherical element distributions. **Table 7** presents a summary of the velocity and heat transfer measurements for the conical element distributions. In this section, the velocity boundary layer measurements are discussed first. Observations of the surface temperature patterns are beifly discussed, and then the heat transfer enhancement results are discussed.

Integral Boundary Layer Parameter Results

Figure 5 presents the integral boundary layer parameters for both distributions relative to the mean elevation. Most interesting from Figure 5 are the observations that as the freestream velocities increase above 15 m/s, the displacement and momentum thicknesses begin to increase. This behavior is the result of the flow not having sufficent space to fully adapt the change in surface condition and by the different local drag behaviors of the cone and hemispherical elements as they protrude deeper into the boundary layer at higher Reynolds numbers.

Surface Temperature Results

Figure 6 and **Figure 7** present contours of θ_R over the test plate surfaces for three different velocities, where

$$\theta_R = \frac{T_R - \overline{T}}{T_\infty - \overline{T}} \tag{9}$$

In each contour, the center most roughness element is the element at the center of the IR image and the flow is from bottom to top. Figure 6 provides a comparison of θ_R contours for the hemispherical distribution, while Figure 7 presents the same comparison for the conical test plate.

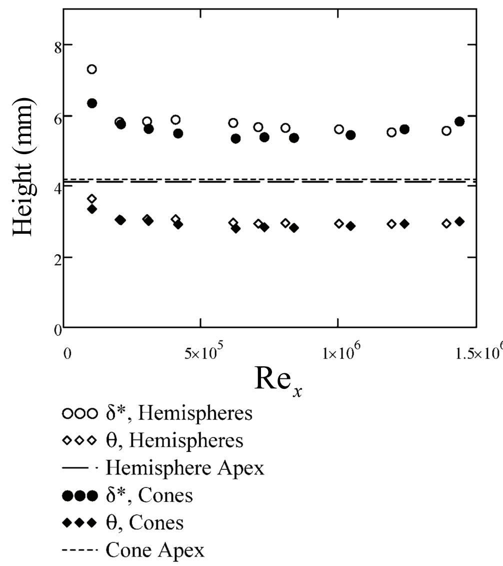

Figure 5: Hemispherical and Conical Integral Boundary Layer Parameters

Figures 6 and 7 demonstrate the significant difference in surface temperatures experienced by the different thermal conductivity elements. The high thermal conductivity of aluminum elements causes the surface temperatures to be greater and far more uniform than those of the plastic elements. Surprisingly, the thermal conductivity of the elements shows little influence on the thermal patterns on the floor of the roughness distributions. At each velocity presented, the temperature contours in the stagnation regions upstream of the elements, in the high velocity regions beside the roughness elements, and in the reattachment regions behind the roughness elements are very similar. Comparing the distributions with a common roughness shape, the magnitudes of θ_R vary slightly along the floor sections, but the θ_R profiles on the distribution floors appear to be very similar.

Also evident in Figures 6 and 7 is the influence velocity has on surface temperatures. As higher heat transfer rates are introduced, the surface temperatures decrease significantly and θ_R rises. Therefore, the values of θ_R over both the aluminum hemispheres and aluminum cones are lower and nearly constant over the apices. However, the sharp peaks of the aluminum cones also produce an interesting effect. At very high velocities, the high heat transfer rate cools the very thin tips and locally increases θ_R.

Convective Enhancement Result

Figure 8 presents the measured Stanton numbers compared to a smooth correlation given by Eq. (3). The Stanton numbers follow the trend of the smooth correlation. While there is a significant offset between the values, the increased convection coefficients exhibited are expected given the level of roughness present on the test plates.

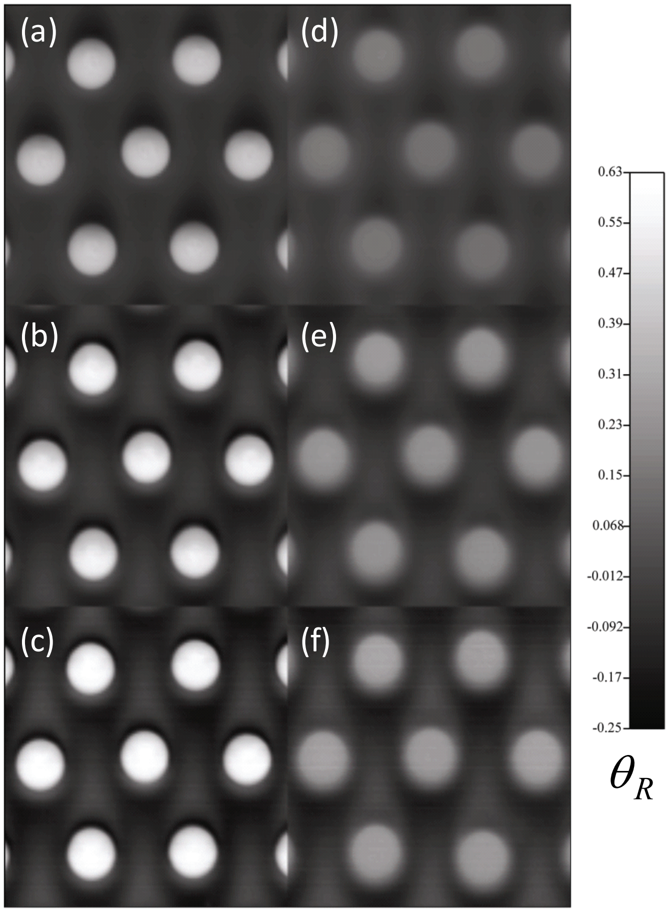

Figure 6. Surface Contours of Theta over the Hemispherical Test Plates for ABS Plastic at (a) 2.5 m/s, (b) 15 m/s, and (c) 35 m/s and Aluminum at (d) 2.5 m/s, (e) 15 m/s, and (f) 35 m/s. Flow direction is from bottom to top.

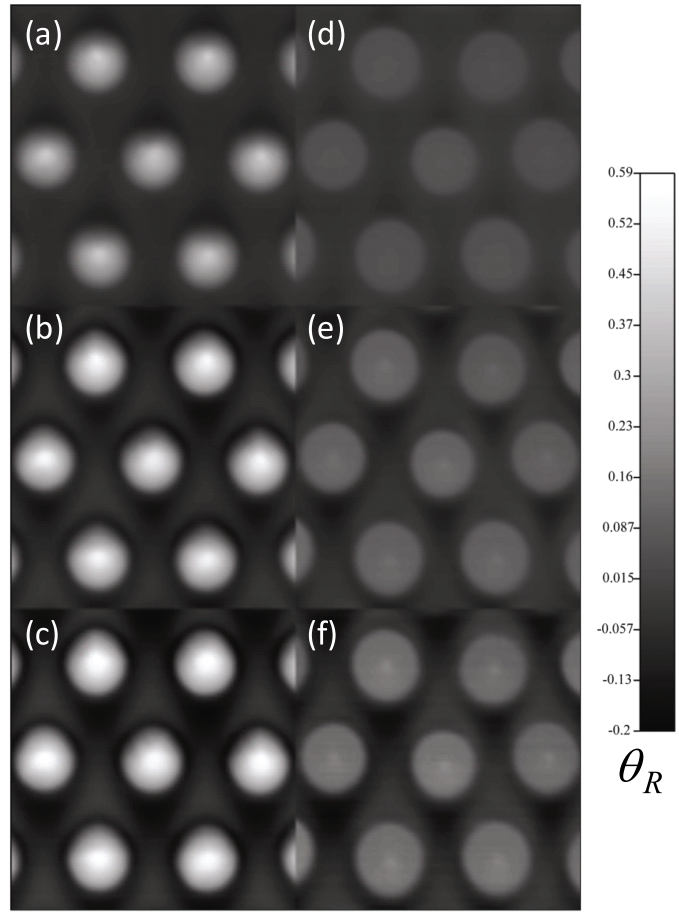

Figure 7. Surface Contours of Theta over the Conical Test Plates for ABS Plastic at (a) 2.5 m/s, (b) 15 m/s, and (c) 35 m/s and Aluminum at (d) 2.5 m/s, (e) 15 m/s, and (f) 35 m/s. Flow direction is from bottom to top.

Figures 9 and **Figure 10** present the Stanton number ratio comparison for the hemispherical and conical test plates, respectively. In determining the Stanton number ratios, the smooth surface Nusselt correlation, Eq. (3), was used to determine the smooth surface Stanton numbers. The measured Stanton numbers for a smooth surface were generally within the measured uncertainty. However, there were significant differences in the Reynolds numbers for each of the rough cases studied and for the smooth plate cases even though nominal freestream velocities were identical. Consequently, the measured Stanton numbers for the roughness distributions was compared to the values predicted by the correlation to determine enhancement values.

In Figure 9, a difference in the Stanton number ratios for Reynolds numbers below $1x10^6$ is observable for the hemispherical element distributions. As expected from the previous measurements of McClain et al. [12], the thermal conductivity of the roughness has a significant impact on the heat transfer rate. However, for the higher Reynolds number tests, the Stanton number ratios collapse. The lack of enhancement of the aluminum hemispherical elements over the plastic elements is caused by 1) the sparse spacing of the roughness elements on the plate and 2) the increasing local roughness element convection coefficients lowering the “fin efficiencies” of the roughness element. In other words, for the hemispherical distributions, the elements are sparsely spaced such that the dominant enhancement mechanism is the enhancement on the floor of the plate. As demonstrated in Figure 6, for the hemispherical elements the dimensionless temperatures on floors of the surfaces are very similar. While the roughness element temperatures in Figure 6 are vastly different, the difference in distribution enhancement is negligible. Thus at high Reynolds numbers, the thermal conductivity of the elements becomes irrelevant to the overall rates of convection compared to the enhancement on the floors of the surfaces.

Table 3. Infrared Test Measurements for Hemispherical Element Test Plates (A_p = 0.250 m^2)

	Aluminum Hemispheres					Plastic Hemispheres				
$U_{\infty,nom}$ (m/s)	E (Volts)	I (Amps)	T_∞ (K)	$\overline{T}$ (K)	T_P (K)	E (Volts)	I (Amps)	T_∞ (K)	$\overline{T}$ (K)	T_P (K)
2.5	10.46	12.43	294.95	312.76	302.28	10.18	12.08	294.45	311.66	304.15
5.0	10.37	12.70	294.77	305.86	298.05	10.10	11.93	294.46	305.70	298.18
7.5	10.34	12.70	294.73	303.20	296.62	10.07	11.98	294.57	303.28	296.97
10.0	10.32	12.69	294.79	301.77	295.89	10.07	12.08	294.69	301.86	296.12
15.0	13.56	17.23	293.89	303.58	295.44	13.52	17.54	294.80	304.57	296.35
17.5	13.54	17.25	294.02	302.78	295.33	13.51	17.55	295.19	304.06	296.40
20.0	13.52	17.25	294.01	302.16	295.19	13.50	17.59	295.41	303.62	296.52
25.0	13.51	17.24	294.13	301.23	295.12	13.49	17.63	295.96	302.94	296.70
30.0	13.50	17.22	294.83	301.11	295.54	13.48	17.64	296.75	302.83	297.13
35.0	13.50	17.23	295.55	301.10	296.06	13.47	17.64	297.84	303.25	297.99

Table 4. Infrared Test Measurements for Conical Element Test Plates (A_p = 0.165 m^2)

	Aluminum Cones					Plastic Cones				
$U_{\infty,nom}$ (m/s)	E (Volts)	I (Amps)	T_∞ (K)	$\overline{T}$ (K)	T_P (K)	E (Volts)	I (Amps)	T_∞ (K)	$\overline{T}$ (K)	T_P (K)
2.5	7.70	13.47	294.27	315.37	305.01	7.69	13.61	293.27	314.27	303.57
5.0	7.63	13.49	294.57	308.15	298.70	7.63	13.60	293.41	307.62	298.26
7.5	7.61	13.53	294.69	305.50	297.40	7.61	13.55	293.35	304.50	296.51
10.0	7.60	13.55	294.72	303.82	296.62	7.60	13.58	293.37	302.73	295.70
15.0	11.15	19.74	294.99	309.80	297.64	11.09	19.69	293.38	308.54	296.68
17.5	11.14	19.73	295.16	308.55	297.41	11.06	19.70	293.49	307.20	296.14
20.0	11.13	19.77	295.37	307.62	297.28	11.04	19.70	293.61	306.11	295.87
25.0	11.11	19.75	295.77	306.37	297.23	11.03	19.72	294.05	304.91	295.67
30.0	11.16	19.83	296.88	305.82	297.58	11.05	19.77	295.22	304.31	296.24
35.0	11.18	19.82	297.86	305.94	298.31	11.08	19.74	296.13	304.29	296.77

Table 5. Measured Convection Coefficients and Uncertainties

	Al Hemispheres		Plastic Hemispheres		Al Cones		Plastic Cones	
$U_{\infty,nom}$ (m/s)	$\bar{h}$ $\left(\frac{\mathrm{W}}{\mathrm{m^2K}}\right)$	$U_{\bar{h}}$ $\left(\frac{\mathrm{W}}{\mathrm{m^2K}}\right)$	$\bar{h}$ $\left(\frac{\mathrm{W}}{\mathrm{m^2K}}\right)$	$U_{\bar{h}}$ $\left(\frac{\mathrm{W}}{\mathrm{m^2K}}\right)$	$\bar{h}$ $\left(\frac{\mathrm{W}}{\mathrm{m^2K}}\right)$	$U_{\bar{h}}$ $\left(\frac{\mathrm{W}}{\mathrm{m^2K}}\right)$	$\bar{h}$ $\left(\frac{\mathrm{W}}{\mathrm{m^2K}}\right)$	$U_{\bar{h}}$ $\left(\frac{\mathrm{W}}{\mathrm{m^2K}}\right)$
2.5	18.24	0.68	18.26	0.71	18.55	0.93	18.16	0.91
5.0	34.57	1.18	30.65	1.08	32.65	1.45	30.34	1.36
7.5	48.01	1.71	42.23	1.41	43.83	1.85	41.07	1.76
10.0	60.18	2.30	53.31	1.74	54.11	2.27	51.05	2.17
15.0	78.23	2.30	74.12	2.32	74.71	2.13	70.13	2.02
17.5	87.51	2.63	82.69	2.66	83.81	2.38	78.47	2.26
20.0	94.81	2.89	90.21	2.96	92.91	2.62	87.12	2.50
25.0	110.44	3.49	108.24	3.78	109.14	3.09	102.08	2.94
30.0	126.10	4.19	125.39	4.69	132.70	3.81	124.66	3.69
35.0	144.40	5.07	142.23	5.68	148.05	4.32	140.32	4.27

Figure 10 shows that for the conical element surfaces, the Stanton number ratios for the aluminum plate are always higher than those of the ABS plastic. The conical plates were constructed with a smaller spacing-to-base-diameter ratio (1.574 compared to 2.099 for the hemispheres). This denser distribution used approximately twice the number of roughness elements as the hemispherical plates. Thus, the heat transfer enhancement on the distribution floor does not dominate the protuberance heat transfer rates for the conical element distributions.

Table 6. Summary of Reduced Measurements for the Hemispherical Element Distributions

$U_{\infty,nom}$	$Re_{x,nom}$	Re_θ	δ	δ^*	θ_M	St_{Al}	St_{Pl}
2.5	90000	626	26.68	7.29	3.63	0.006548	0.006114
5	195000	1034	24.63	5.80	3.04	0.005711	0.005074
7.5	298000	1547	24.71	5.81	3.05	0.005248	0.004645
10	396000	2073	24.52	5.87	3.05	0.004982	0.004398
15	595000	3043	24.56	5.77	2.96	0.004318	0.004109
17.5	698000	3453	24.68	5.66	2.93	0.004094	0.003925
20	801000	3957	24.43	5.63	2.94	0.003889	0.003729
25	999000	4886	24.61	5.59	2.93	0.003628	0.003597
30	1199000	5799	24.97	5.51	2.92	0.003467	0.003474
35	1380000	6795	24.34	5.55	2.93	0.003390	0.003379

Table 7. Summary of Reduced Measurements for the Conical Element Distributions

$U_{\infty,nom}$	$Re_{x,nom}$	Re_θ	δ	δ^*	θ_M	St_{Al}	St_{Pl}
2.5	96000	538	24.85	6.33	3.34	0.005979	0.005875
5	193000	976	25.33	5.73	3.02	0.005374	0.005008
7.5	292500	1436	26.23	5.60	3.00	0.004827	0.004533
10	395000	1872	25.14	5.48	2.91	0.004439	0.004223
15	580000	2700	24.43	5.33	2.79	0.004118	0.003867
17.5	680000	3187	25.41	5.37	2.83	0.003966	0.003726
20	780000	3634	25.94	5.35	2.81	0.003842	0.003620
25	975000	4609	26.52	5.43	2.86	0.003635	0.003395
30	1170000	5593	25.95	5.59	2.92	0.003667	0.003455
35	1360000	6643	26.10	5.81	2.99	0.003527	0.003333

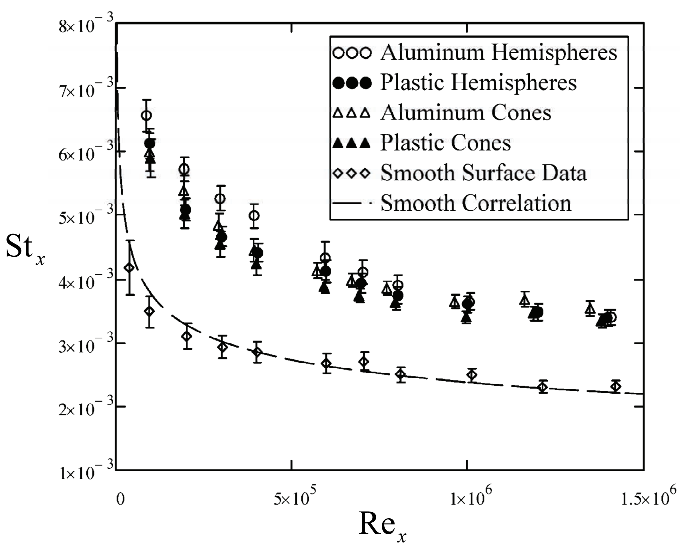

Figure 8: Test Plate Stanton Numbers Compared to the Smooth Correlation

To better distinguish the enhancement differences for the two plate geometries, an enhancement difference for each plate and each average Reynolds number were explored. The enhancement difference was defined as

$$\Delta E = \left(\frac{St_R}{St_S}\right)_{AL} - \left(\frac{St_R}{St_S}\right)_{PL} \tag{10}$$

An uncertainty in the enhancement difference was also determined. The enhancement difference and its uncertainty may be used in the same principle as a statistical null variable test. That is, if for two measurements, the uncertainty in the difference is greater than the difference between the two measurements, then the difference between the two measurements is not statistically meaningful [17].

Figure 11 shows the enhancement difference for the hemispherical and conical test plates. For the hemispherical distributions, there is a significant and measurable difference between the Stanton number ratios up to a Reynolds number of $1x10^6$. At low Reynolds numbers, the difference in the enhancement for the hemispherical distributions is a maximum of 22% of the smooth surface rate of convection. For Reynolds numbers over $1x10^6$, a significant difference between the plastic and aluminum enhancement values is not observed.

For the conical distributions, with the exception of the lowest Reynolds number tested, there is a quantifiably greater enhancement from the aluminum distribution at all test speeds. For the conical surface tested, the enhancement for the aluminum distribution is on average 12% of the smooth surface flux higher than the enhancement for the plastic distribution. This percentage enhancement is lower than the enhancement difference expected from the measurements and predictions of McClain et al [12]. While the conical element of this study are more tightly packed than the hemispherical elements studied, the spacing to diameter ratio is still much less than for the surfaces studied by McClain et al. [12]. As the packing density increases for the conical element distributions, the influence of the enhancement of the surface floors is further reduced, and the enhancement difference would also be expected to increase.

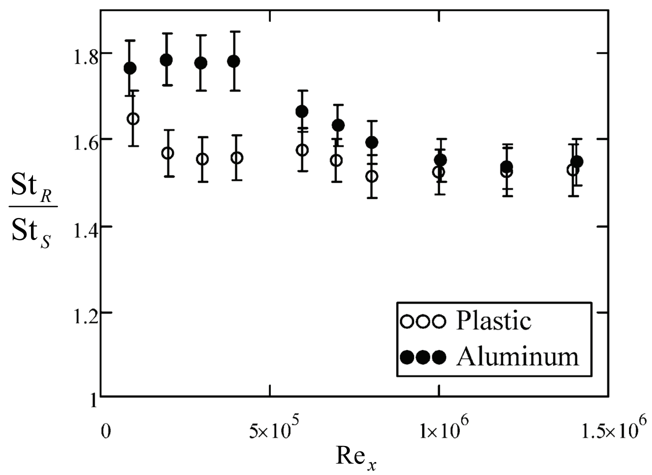

Figure 9. Stanton Number Ratios of the Two Hemispherical Roughness Distribution Plates

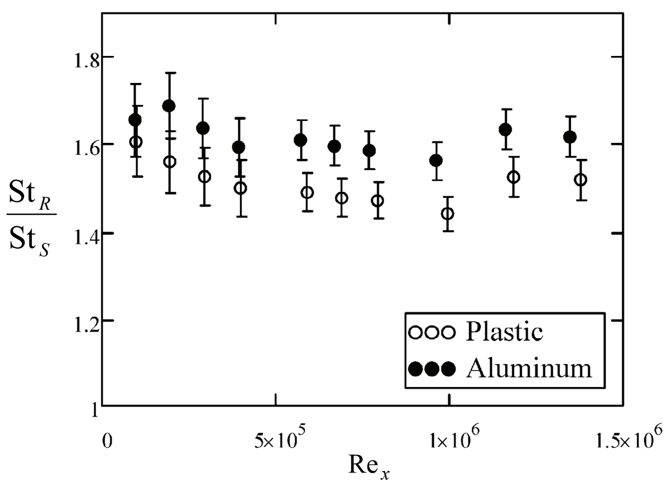

Figure 10. Stanton Number Ratios of the Two Conical Roughness Distribution Plates

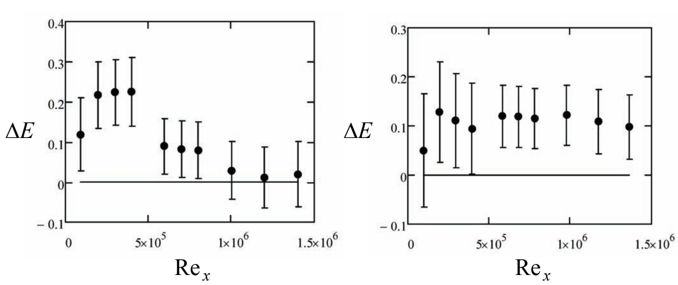

Figure 11. Uncertainty Based Comparison of the Difference in Stanton Number Enhancement for the Hemispheres (left) and Cones (right)

CONCLUSIONS

An experimental investigation of the effects of roughness element thermal conductivity on distribution convection enhancement was conducted. The surfaces chosen were surfaces of ordered deterministic shapes but with characteristics such as element-height to chord ratios and Sigal-Danberg parameters similar to the characteristics exhibited by gas-turbine surfaces roughened by foreign material deposition. The primary conclusions of the study are:

1) The element thermal conductivity plays a significant role in determining the roughness element temperatures. However, the temperature patterns on the floors of the surfaces were very similar for each respective roughness geometry.

2) For surfaces with sparsely spaced elements, the thermal conductivity of the roughness elements is significant at low Reynolds numbers. As the Reynolds number increases, the dominant mode of convective enhancement becomes the enhancement on the surface floor and the importance of the roughness thermal conductivity decreases.

3) For the cone surface with a more densely packed distribution of elements, the thermal conductivity of the elements was significant for all but one of the Reynolds numbers used in the investigation. This effect implies that as elements are more densely packed, the enhancement on the floors of the surfaces becomes less important in determining the distribution enhancement.

The results also represent a significant calibration set for future development of methods to predict convective heat transfer enhancement of rough surfaces. Future efforts are planned that include 1) comparing the measurements presented in this study to predictions from the discrete-element model, 2) investigating the local heat transfer coefficients along the surfaces of the roughness elements by combining surface temperature measurements with an inverse steady state conduction approach, and 3) performing similar convection enhancement measurements using surfaces with randomly-rough distributions of different thermal conductivities.

NOMENCLATURE

A	=	Thermal logarithmic region intercept
A_p	=	Plan form area of heated section of test plate
B	=	Velocity logarithmic region intercept
C_f	=	Skin friction coefficient
D	=	Protuberance base diameter
d	=	Local diameter of protuberance at a given elevation
E	=	Measured voltage across thin-film Mylar sheet
Fr_x	=	Frossling number based on distance from knife-edge of the plate $\left(Nu_x / \sqrt{Re_x}\right)$

I = Measured current through thin-film Mylar sheet
N = Number of repeated measurements to evaluate a mean measurement
Nu_x = Nusselt number based on distance from knife-edge of the plate
Pr = Prandtl number of air at film temperature
Pr_t = turbulent Prandtl number
Re_x = Reynolds number based on distance from knife-edge of the plate
Re_θ = Reynolds number based on the momentum thickness
S = Measurement standard deviation
St_R = Stanton number for the roughness distribution
St_S = Stanton number from the smooth correlation, Eq. (3)
$\overline{T}$ = Average infrared image temperature (that is, the arithmetic mean of all pixel temperature values)
T_∞ = Freestream temperature of the fluid
T_P = Plexiglass bottom-side surface temperature
T_R = Local temperature measured along the rough surface
t = Student's-t value
t_M = Mylar thickness (= 0.185 mm)
t_P = Plexiglas thickness (= 19.05 mm)
$\overline{h}$ = Average convective heat transfer coefficient
k = Roughness element apex elevation above plate floor
k_{eff} = Roughness element apex elevation above distribution "melt-down" height (k-Δy_m)
k_M = Thermal conductivity of the Mylar (≈ 0.083 W/m·K)
k_P = Thermal conductivity of the Plexiglas (= 0.18 W/m·K)
k_R = Thermal conductivity of the roughness elements
k^+ = the inner variable height evaluated at the apices of the roughness elements
u = component of flow along the primary wind tunnel axis
u^* = friction velocity, $\sqrt{\frac{\tau_w}{\rho}}$ or $U_\infty\sqrt{\frac{C_f}{2}}$
u^+ = normalized inner variable velocity (u/u^*)
y = Elevation from the plate floor
y' = the elevation from the mean or "melt-down" height, (y-Δy_m)
y^+ = inner variable height $\left(\frac{yu^*}{\nu}\right)$
α = thermal diffusivity of air at film temperature (m^2/s)
β = volumetric thermal expansion coefficient (1/K)
δ = viscous boundary layer thickness
δ^* = displacement thickness
Δy_m = Height of the mean elevation above the plate floor
Λ_{eff} = Modified Sigal-Danberg parameter
ξ = Roughness frictional offset height
θ_M = Momentum thickness
θ_R = Dimensionless temperature over element and surface
κ = von Karman's constant
ρ = fluid density
ε = emissivity of the Mylar surface (= 0.95)
ν = kinematic viscosity of air
σ = Stefan-Boltzmann constant
μ = molecular viscosity

Subscripts
AL = Aluminum elements
cal = value assocated with measurements performed during *in-situ* calibration
$meas$ = value associated with measurements performed during testing
PL = Plastic Elements
R = Rough
S = Smooth

ACKNOWLEDGMENTS

The authors thank Dr. William Jordan and the Mechanical Engineering Department at Baylor University for their support of these activities. The authors also thank Dr. Kenneth Van Treuren and Mr. Jason Gregg for their valuable input and collaborative efforts throughout this process. Finally, the authors thank Ashley Orr and Gilberto Narvaez III for their help with test plate construction, traversing system automation, and LabVIEW programming.

REFERENCES

[1] Bons, J. P., Taylor, R., McClain, S., and Rivir, R. B., 2001, "The Many Faces of Turbine Surface Roughness," *ASME J. Turbomach.*, **123**(4), pp. 739–748.
[2] Taylor, R. P., 1990, "Surface Roughness Measurements on Gas Turbine Blades," *ASME J. Turbomach.*, **112**(1), pp. 175–180.
[3] Tarada, F., and Suzuki, M., 1993, "External Heat Transfer Enhancement to Turbine Blading due to Surface Roughness," ASME Paper No. 93-GT-74.
[4] Taylor, R.E., 1998, "Thermal Conductivity Determinations of Thermal Barrier Coatings," *Materials Science and Engineering A*, 245, pg 160-167.
[5] Schultz, U., Leyens, C., Fritscher, K., Peters, M., Saruhan-Brings, B., Livinge, O., Dorvaux, J.-M., Poulain, M., Mevrel, R., and Caliez, M. 2003, "Some Recent Trends in Research and Technology of Advanced Thermal Barrier Coatings," *Aerospace Science and Technology*, 7, pg 73-80.
[6] Almeida, D. S., Silva, C.R.M., Nono, M.C.A., Cairo, C.A.A., 2007, "Thermal Conductivity Investigation of Zirconia Co-doped with Yttria and Niobia EB-PVD TBCs," *Materials Science and Engineering A*, 443, pg 60-65.
[7] ASM International, 1990, *Metals Handbook: Properties and Selection: Irons, Steels, and High Performance Allows*, Tenth Ed.
[8] Schlichting, H., 1936, "Experimental Investigation of the Problem of Surface Roughness," NACA TM-832, National Advisory Committee on Aeronautics.
[9] Finson, M. L., 1982, "A Model for Rough Wall Turbulent Heating and Skin Friction," AIAA Paper 82-0199.
[10] Taylor, R. P., 1983, "A Discrete Element Prediction Approach for Turbulent Flow over Rough Surfaces," Ph.D. Dissertation, Department of Mechanical and Nuclear Engineering, Mississippi State University.
[11] Bons, J. P., McClain, S. T., Wang, Z. J., Chi, X., and Shih, T. I., 2008, "A Comparison of Approximate vs. Exact Geometrical Representations of Roughness for CFD Calculations of Cf and St," *Journal of Turbomachinery*, Vol. 130, No. 2, 021024.
[12] McClain, S. T., Hodge, B. K., and Bons, J. P., 2011, ""The Effect of Element Thermal Conductivity on Turbulent Convective Heat Transfer from Rough Surfaces," *Journal of Turbomachinery*, Vol. 133, 021024.
[13] Boyle, R. J., and Senyitko, R. G., (2005), "Effect of Surface Roughness on Turbine Vane Heat Transfer", ASME Paper No. GT2005-68133.

[14] Sigal, A. and Danberg, J. E., (1990), "New Correlation of Roughness Density Effect on the Turbulent Boundary Layer," AIAA Journal, Vol. 28, No. 3, pp. 554-556.
[15] McClain, S. T., Collins, S. P., Hodge, B. K., and Bons, J. P., (2006), "The Importance of the Mean Elevation in Predicting Skin Friction for Flow over Closely Packed Surface Roughness," Journal of Fluids Engineering, Vol. 128, No. 3, pg 579-586.
[16] FLIR, (2010) "ThermoVision® SC4000: Science-Grade Infrared Camera," www.flir.com.
[17] Coleman, H. W. and Steele, W. G., (1999), *Experimentation and Uncertainty Analysis for Engineers*, Second Edition, John Wiley and Sons, Inc.
[18] Kline, S. J., and McClintock, F. A., (1953), "Describing Uncertainties in Single-Sample Experiments," *Mechanical Engineering*, Vol. 75, pg 3-8.
[19] Incropera, F., Dewitt, D., Bergman, T., Lavine, A., (2007), *Fundamentals of Heat and Mass Transfer*, 6th ed., John Wiley & Sons, Inc., Hoboken, NJ.
[20] Mart, S. R. and McClain, S. T., (2011), "Protuberances in a Turbulent Thermal Boundary Layer," Submitted for presentation at the 2011 ASME TurboExpo, June 6-10, 2011, Vancouver, Canada, GT2011-45180.
[21] Bejan, A., (2004), *Convection Heat Transfer*, Wiley & Sons, Inc., 2nd Ed.
[22] Clauser, F. H., 1954, ''Turbulent Boundary Layers in Adverse Pressure Gradients,'' J. Aeronaut. Sci., 21, pp. 91–108.
[23] Coleman, H. W., Hodge, B. K., and Taylor, R. P., (1984), "A Re-Evaluation of Schlichting's Surface Roughness Experiment," *Journal of Fluids Engineering*, 106, pp. 60–65.